Draft version October 17, 2025
Typeset using LaTeX twocolumn style in AASTeX7

Demonstrating Exoplanet Transit Photometry from Space with a 15-mm Aperture Optical Navigation Camera on Hayabusa2

Koki Yumoto [1,2] Toru Kouyama,[3] Manabu Yamada,[4] Yuya Mimasu [2] Tomokatsu Morota,[5] Yuichiro Cho [5] Yasuhiro Yokota [2,6] Masahiko Hayakawa,[2] Anthony Arfaux [1] Eri Tatsumi,[2,7,8] Moe Matsuoka,[9] Naoya Sakatani [2] Sumito Shimomura,[2] Shingo Kameda,[10] Satoshi Tanaka,[2] Keigo Enya,[2] and Seiji Sugita [5,4]

[1] *LIRA, Observatoire de Paris, Université PSL, Sorbonne Université, Université Paris-Cité, CY Cergy Paris Université, CNRS, Meudon, France*

[2] *Institute of Space and Astronautical Science, Japan Aerospace Exploration Agency, Sagamihara, Kanagawa, Japan*

[3] *Artificial Intelligence Research Center, National Institute of Advanced Industrial Science and Technology, Koto, Tokyo, Japan*

[4] *Planetary Exploration Research Center (PERC), Chiba Institute of Technology, Narashino, Chiba, Japan*

[5] *Department of Earth and Planetary Science, The University of Tokyo, Bunkyo, Tokyo, Japan*

[6] *Institute of Science Tokyo, Ookayama, Tokyo, Japan*

[7] *Instituto de Astrofísica de Canarias (IAC), University of La Laguna, La Laguna, Tenerife, Spain*

[8] *Department of Astrophysics, University of La Laguna, La Laguna, Tenerife, Spain*

[9] *Geological Survey of Japan (GSJ), National Institute of Advanced Industrial Science and Technology, Tsukuba, Ibaraki, Japan*

[10] *Department of Physics, Rikkyo University, Toshima, Tokyo, Japan*

ABSTRACT

Observations of exoplanet transits by small satellites have gained increasing attention for reducing detection biases. However, no unambiguous detection of an exoplanet has yet been demonstrated using optics with apertures smaller than 60 mm. Here, we investigated the detectability of exoplanet transits using the telescopic Optical Navigation Camera (ONC-T) onboard the Hayabusa2 spacecraft, which has an effective aperture of only 15 mm. We conducted transit observations of the hot Jupiters WASP-189 b and MASCARA-1 b, collecting data for ten and four events, respectively. The transit signal was detected with a signal-to-noise ratio (SNR) of 13 for WASP-189 b and 8 for MASCARA-1 b for each event. Stacking all events improved the SNR to 40 and 16, respectively. The transit mid-times of each event were measured with a precision of 6 minutes and were consistent with Transiting Exoplanet Survey Satellite (TESS) data to within 2 minutes. The planet-to-star radius ratio was determined with an absolute precision of 0.004 (6% relative) and agreed with TESS results to within 0.002 (3% relative). The recent ONC-T and TESS data enabled an update to the planetary ephemerides. We report a 4σ discrepancy between the updated orbital period of MASCARA-1 b and previously reported values. ONC-T sets a new record for the smallest-aperture instrument to detect an exoplanet transit from space, advancing the frontier of exoplanet science with miniature instrumentation. Our results suggest that optics as small as ONC-T may be capable of detecting transiting long-period Jupiters: a population that remains underrepresented in current surveys.

Keywords: Transit photometry (1709) — Exoplanet detection methods (489) — Photometer (2030) — Transit instruments (1708) — Light curves (918) — Hot Jupiters (753)

1. INTRODUCTION

Despite the discovery of over 5,000 exoplanets, those with orbits and masses similar to planets in our Solar System remain limited in number; most known exoplanets have larger masses or shorter orbital periods (Fig. 1a). This apparent absence may be largely driven by observational biases (e.g., D. Foreman-Mackey et al. 2016). Radial velocity (RV) surveys are capable of detecting planets with year-long orbits, since they do not necessitate dense temporal sampling across the full orbital period. However, their sensitivity is generally limited to planets more massive than approximately one Jupiter mass, due to the weak RV signals exerted by lower-mass planets (V. I. Ananyeva et al. 2022). In contrast, transit observations can detect planets across a broader

Email: kyyumoto@gmail.com

range of sizes, but the current sample likely lacks long-period planets because their detection requires continuous, long-duration time-series data. The number of transiting planets identified to date begins to fall short of that expected for a uniform distribution of exoplanets in $\log_{10}$(Period) space once orbital periods exceed ∼100 days (Fig. 1b). While this apparent deficit could reflect a genuine scarcity of long-period planets, it is more due to observational bias, as RV surveys find a nearly uniform distribution over the $\log_{10}$(Period) domain (A. Cumming et al. 2008). For instance, the *Transiting Exoplanet Survey Satellite* (TESS) observes a given field for only ∼27 days, limiting its ability to detect longer-period planets. Mitigating these biases through additional surveys is essential to assess whether Solar System-like planets are unique and to better understand the formation pathways of habitable planets (National Academies of Sciences, Engineering, and Medicine 2018).

One proposed strategy for reducing these biases is to search for transit signals around bright stars through long-term monitoring with small satellites (e.g., H. Kawahara et al. 2020). The use of small satellites for transit detection has attracted attention owing to their stable, atmosphere-independent performance and the substantial recent reduction in launch costs (E. L. Shkolnik 2018; S. Serjeant et al. 2020). These advantages enable dedicated, long-term monitoring of individual stars (R. M. Millan et al. 2019), and many key technologies have been demonstrated in recent missions. For instance, the 6U CubeSat *Arcsecond Space Telescope Enabling Research in Astrophysics* (ASTERIA) successfully demonstrated the capability of small satellites to maintain long-term pointing and thermal stability (Table 1; M. Smith et al. 2018). The *Bright Target Explorer* (BRITE) constellation, consisting of 20-cm nanosatellites, has demonstrated that deploying a network of nearly identical satellites can significantly improve both temporal and spatial coverage (W. W. Weiss et al. 2021). Building on these demonstrations, the *LOng-period Transiting exoplanet sUrvey Satellite* (LOTUS) being developed at the Japan Aerospace Exploration Agency (JAXA) plans to use a nanosatellite equipped with a 7.5-cm aperture wide-field imager to search for long-period planets that remain undetected (H. Kawahara et al. 2020).

Despite these promising advances in small-satellite technologies, their photometric capability for transit detection has yet to be fully explored. To date, the marginal 2.2σ detection of the super-Earth 55 Cnc e by ASTERIA, equipped with a 60 mm aperture optics, remains the most compact optical system to yield

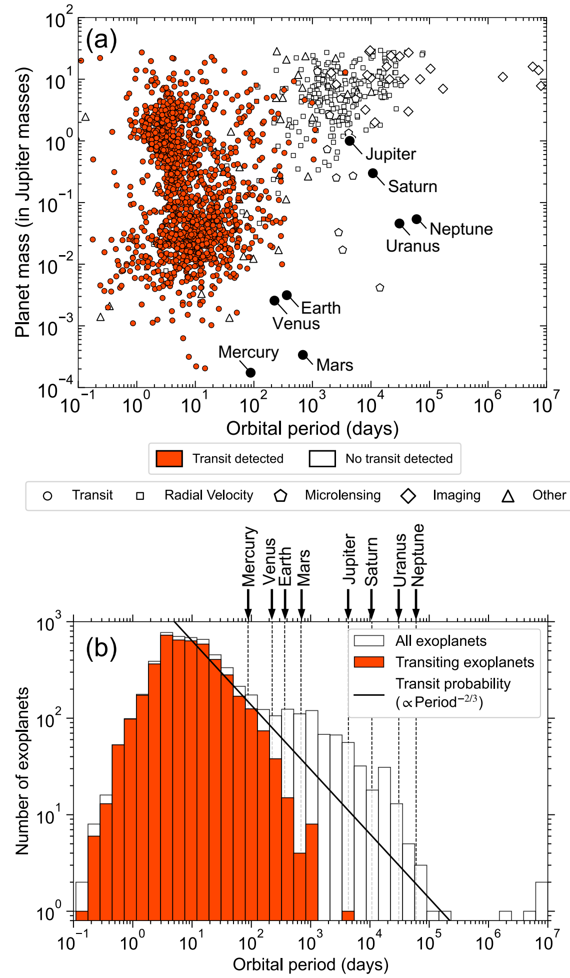

Figure 1. Population statistics of all 5,917 confirmed exoplanets as of 11 June 2025. **(a)** Orbital period vs. planet mass for all planets with direct mass estimates. Red filled symbols represent exoplanets with transit detections, while white open symbols denote those without. Marker shapes indicate the method of discovery. **(b)** Distribution of orbital periods for all known exoplanets and transiting exoplanets. The black solid line represents the transit probability, proportional to Period$^{-2/3}$, scaled to match the data at a 10-day period. This line represents the expected distribution of transiting exoplanets, under the assumption that planet occurrence is uniform in $\log_{10}$(Period) space. Data are from the NASA Exoplanet Archive.

a credible transit signal, while no unambiguous detection has been reported with smaller aperture optics (Table 1). Several transit-like signals have been identified with the 30-mm aperture of BRITE (L.-C. Yeh & I.-G. Jiang 2020; A. Fuentes & M. Solar 2024) and the 16-mm aperture of *Solar Terrestrial Relations Observatory/Heliospheric Imager-1A* (STEREO/HI-1A; K. T. Wraight et al. 2011; G. N. Whittaker 2014), but it remains uncertain whether these signals originate from actual exoplanet transits. For instance, the transit-like sig-

Table 1. Performance metrics of miniature optics applied to exoplanet transit observations.

Instrument	Wavelength	Plate scale	Aperture	Detector temperature stability	Pointing stability	Transit detections
Hayabusa2/ ONC-T	400–950 nm(1)	22.1" pixel^{-1}(1)	15 mm(1)	2–4°C (RMSD)(2)	6–17" (RMSD)(2)	Detected transits of two known hot Jupiters(2).
STEREO/ HI-1A	630–730 nm(3)	35" pixel^{-1}(3)	16 mm(3)	Passively cooled to ∼ −80°C(4)	7″ (RMSD)(3)	Found transit candidates (follow-up required)(3,5).
BRITE constellation	400–450 nm or 550–700 nm(6)	27–30" pixel^{-1}(6)	3 cm(6)	∼4°C drift per orbit(7,a)	45" (RMSD)(8)	Found transit candidates (follow-up required)(9,10). No detection in the β Pictoris system(11).
PicSat	400–680 nm(12)	4.2" pixel^{-1}(13,b)	3.7 cm(12)	0.004°C (RMSD)(14)	30" (RMSD)(12,c)	No data due to attitude failure(14).
ASTERIA	500–900 nm(15)	15.8" pixel^{-1}(15)	6.07 cm(15)	±0.01°C (max–min)(15)	0.5" (RMSD)(15)	Marginal detection of 55 Cancri e(16). No detection in the α Centauri A and B systems(17).
TESS	600–1000 nm(18)	21" pixel^{-1}(18)	10.5 cm(18)	<0.02°C per day(19)	<2.0" (3σ)(20)	Detected >7000 transits including candidates(e.g., 21).
CUTE	247.9–330.6 nm (0.39 nm steps)(22)	2.5" pixel^{-1}(22)	20.6 × 8.4 cm(22)	±2°C (max–min)(23)	<6" (RMSD)(23)	Detected the transit spectrum of WASP-189 b(24).
MOST	380–700 nm(25)	3" pixel^{-1}(25)	15 cm(25)	±0.1°C(25)	3–5" (RMSD)(26)	Detected transits in multiple systems(e.g., 27,28).

Note—(a) The magnitude of the drift varies depending on the satellite's orientation relative to the Sun.
(b) Defined by the 3 µm diameter of the fiber core.
(c) Additional photometric stability is achieved through fine adjustments of the fiber head position within the focal plane.
References: (1) S. Kameda et al. (2017); (2) This study; (3) K. T. Wraight et al. (2011); (4) C. J. Eyles et al. (2009); (5) G. N. Whittaker (2014); (6) W. W. Weiss et al. (2021); (7) A. Popowicz (2018); (8) K. Sarda et al. (2014); (9) L.-C. Yeh & I.-G. Jiang (2020); (10) A. Fuentes & M. Solar (2024); (11) M. Mol Lous et al. (2018); (12) V. Lapeyrere et al. (2017); (13) M. Nowak et al. (2017); (14) M. Nowak et al. (2018); (15) M. Smith et al. (2018); (16) M. Knapp et al. (2020); (17) A. Krishnamurthy et al. (2021); (18) G. R. Ricker et al. (2015); (19) R. Vanderspek et al. (2018); (20) T. Nguyen et al. (2018); (21) E. S. Ivshina & J. N. Winn (2022); (22) K. France et al. (2023); (23) A. Egan et al. (2023); (24) A. G. Sreejith et al. (2023); (25) G. Walker et al. (2003); (26) S. Grocott et al. (2004); (27) J. N. Winn et al. (2011); (28) E. Miller-Ricci et al. (2008).

nal of HD 213597 detected by STEREO/HI-1A was later found to be an eclipsing binary (P. Chaturvedi et al. 2014), while other candidates lack sufficient follow-up data for confirmation. The lack of unambiguous transit detections by BRITE and STEREO/HI-1A does not necessarily indicate limitations of small-aperture optics, as their observations were neither targeted at nor timed to capture well-characterized exoplanets. Thus, optics with apertures smaller than 60 mm may still be viable for transit detection, and their sensitivity to transit signals needs to be quantified to assess the capabilities of future small-satellite missions.

To address this issue, we conducted transit observations of two known hot Jupiters using the *telescopic Optical Navigation Camera* (ONC-T) onboard the Hayabusa2 spacecraft: an asteroid sample return mission led by JAXA. With an effective aperture of just 15 mm, ONC-T represents, to our knowledge, the smallest aperture ever used for transit observations from space (Table 1). Its pointing and thermal stability are comparable to those demonstrated by previous small satellite missions such as BRITE and CUTE, with ASTERIA exhibiting even greater stability (Table 1). In addition, ONC-T exhibits a high number of hot pixels resulting from its 10 years of operation (T. Kouyama et al. 2021), simulating the degraded detector conditions that future missions may experience after long-term operations. These features make ONC-T a unique space-based photometer for studying the scientific potential of compact optics deployable on CubeSats and nanosatellites. In this study, we assess the detectability of transits by ONC-T and evaluate the measurement accuracy of transit depths and timings by comparing the results with those from TESS and previous observations.

2. OBSERVATIONS

2.1. *Telescopic Optical Navigation Camera (ONC-T) onboard Hayabusa2*

ONC-T is a multi-band, shutter-less charge-coupled device (CCD) imager used for both scientific observations and onboard navigation. It played a crucial role in guiding Hayabusa2 to asteroid (162173) Ryugu and in precisely targeting the sample collection sites (N. Ogawa et al. 2020). The dioptric system of ONC-T has a focal length of 120.5 mm (H. Suzuki et al. 2018) and an effective aperture diameter of 15 mm (S. Kameda et al.

2017). The camera is equipped with a filter wheel containing one panchromatic filter covering the 400–950 nm wavelength range and seven narrow-band filters. The detector is CCD4720AIMO (Teledyne e2v), which has a 1024 × 1024-pixel array with a pixel size of 13 µm and a 100% fill factor, i.e., the entire detector surface is sensitive to light. The detector is passively cooled to −30°C during nominal observations, with temperature stability maintained via an onboard heater. Although ONC-T has operated nominally since launch, the number of hot pixels has increased linearly over time, attributed to cumulative radiation damage to the CCD (T. Kouyama et al. 2021).

Building on the high photometric precision of ONC-T demonstrated over years of operation (K. Yumoto et al. 2024; E. Tatsumi et al. 2019), we launched a campaign to observe exoplanet transits during the extended mission's 10-year space cruise (2021–2031). We focused on observing confirmed exoplanets, where transit timings are predictable. The targets were selected based on their visibility and the expected signal-to-noise ratio (SNR). Hayabusa2 orbits the Sun at approximately 1 AU in the ecliptic plane, completing one revolution per year. In its nominal configuration, the spacecraft is oriented such that the ONC-T boresight points approximately in the anti-solar direction, with a $\sim$10° offset to optimize the influence of solar radiation pressure on spacecraft dynamics (Y. Tsuda et al. 2017). Due to constraints related to spacecraft thermal stability, solar radiation pressure, and stray lights, ONC-T can point within a favorable angular range of ±10°, with a hard limit of ±40°, from the nominal pointing direction. As a result, stars located within ±10° or ±40° of the ecliptic plane are observable, each with an annual visibility window of approximately two weeks to one month. For all confirmed transiting exoplanets within this range, we calculated the predicted SNR of their transit signals (see Section 5 for details on the calculation).

WASP-189 b and MASCARA-1 b were selected based on their high predicted SNR, ranking 2nd and 9th, respectively, among all visible targets. Both planets are ultra-hot Jupiters with $\gtrsim$2 Jupiter masses and dayside temperatures exceeding 3000 K. WASP-189 b orbits a $m_V = 6.6$ star with a 2.7-day period (M. Lendl et al. 2020), and MASCARA-1 b orbits a $m_V = 8.3$ star with a 2.1-day period (M. J. Hooton et al. 2022). These planets also warrant a search for potential transit timing variations (TTVs), as their ephemerides were not updated in the most recent TTV surveys by E. S. Ivshina & J. N. Winn (2022) and A. Kokori et al. (2023), which included data only through 2021 due to the limited availability of recent observations at the time.

We observed 10 transits of WASP-189 b and four transits of MASCARA-1 b over a period of 2.5 years. The observation times and imaging conditions are summarized in Table 2. Each transit was observed continuously for approximately 21 hours, covering at least ±8 hours around the predicted mid-transit time and fully capturing the ingress and egress. The transits were observed using the panchromatic filter to maximize the SNR. For each observation, the spacecraft was oriented to center the target star within the recorded portion of the image and to minimize stray light (E. Tatsumi et al. 2019). The spacecraft attitude was held fixed throughout each observation. The duration of each observation and the interval between successive sessions were constrained by the buildup of solar radiation pressure, caused by the non-optimal spacecraft orientation required during observations; minimizing this load has been essential to maintain attitude control without fuel consumption (Y. Tsuda et al. 2017). The imaging cadence ranged from 65 to 240 seconds, including both the exposure time and the overhead needed to store each image in the onboard data recorder.

2.2. *Transiting Exoplanet Survey Satellite (TESS)*

We analyzed TESS data for WASP-189 b and MASCARA-1 b, acquired within eight months of the ONC-T observations, to validate the ONC-T results. WASP-189 b was observed by TESS in Sector 51 (April 22–May 18, 2022), while MASCARA-1 b was observed in Sectors 55 (August 5–September 1, 2022) and 82 (August 10–September 5, 2024). Transit events without continuous coverage from ingress to egress were excluded, resulting in three usable transits for WASP-189 b and 20 for MASCARA-1 b (9 in Sector 55 and 11 in Sector 82).

3. DATA REDUCTION AND MODELING

3.1. *Light curves from aperture photometry*

The raw ONC-T images were first corrected for bias, dark current, and hot pixels, then divided by the flat-field pattern and normalized by the exposure time:

$$p^t(x,y) = \Big[p^t_{\rm raw}(x,y) - p^t_{\rm bias}(T^t_{\rm CCD}, T^t_{\rm ELE}, T^t_{\rm AE}) - p^t_{\rm dark}(T^t_{\rm CCD}) - p_{\rm hot}(x,y,T_{\rm CCD})\Big] \cdot \frac{1}{t_{\rm exp}\, f(x,y)}. \quad (1)$$

Here, $p^t_{\rm raw}(x,y)$ represents the raw signal intensity (in DN units) of an image taken at time t and pixel coordinates (x,y), while $p^t(x,y)$ denotes the corresponding image after reduction. The exposure time is given by $t_{\rm exp}$ in seconds, and f represents the flat-field pattern

Table 2. List of transit events observed by the Optical Navigation Camera along with their observational conditions.

Event	Planet name	Observation time (UTC)	Imaging cadence (sec)	Exposure time per image (sec)	Number of images
1	WASP-189 b	2022 Dec 17 19:00:27 – 2022 Dec 18 18:58:27	120	44.56	720
2	WASP-189 b	2022 Dec 25 18:30:28 – 2022 Dec 26 18:28:29 $^{(a)}$	120	44.56	702
3	WASP-189 b	2023 Jan 05 18:40:24 – 2023 Jan 06 18:38:25	120	44.56	720
4	WASP-189 b	2023 Jan 08 12:03:24 – 2023 Jan 09 12:01:24	120	44.56	720
5	WASP-189 b	2023 Jan 13 22:48:26 – 2023 Jan 14 19:46:25	120	44.56	630
6	WASP-189 b	2023 Jan 19 09:34:24 – 2023 Jan 20 06:32:25	120	44.56	630
7	WASP-189 b	2023 Jan 22 02:56:25 – 2023 Jan 22 23:54:25	120	44.56	630
8	WASP-189 b	2023 Nov 12 09:00:28 – 2023 Nov 13 06:13:23	65	44.56	1176
9	WASP-189 b	2024 Sep 15 04:00:26 – 2024 Sep 16 01:13:21	65	44.56	1176
10	WASP-189 b	2024 Sep 17 21:00:24 – 2024 Sep 18 18:13:19	65	44.56	1176
11	MASCARA-1 b	2022 Jun 11 10:01:31 – 2022 Jun 12 09:57:31	240	178.26	360
12	MASCARA-1 b	2024 Nov 29 23:01:32 – 2024 Nov 30 20:18:43	200	178.26	384
13	MASCARA-1 b	2024 Dec 04 04:01:31 – 2024 Dec 05 01:18:42	200	178.26	384
14	MASCARA-1 b	2024 Dec 21 09:01:31 – 2024 Dec 22 06:18:42	200	178.26	384

NOTE—(a) Data gap between 22:06:29–22:14:29 and 22:52:29–23:16:29 on 2022 Dec 25.

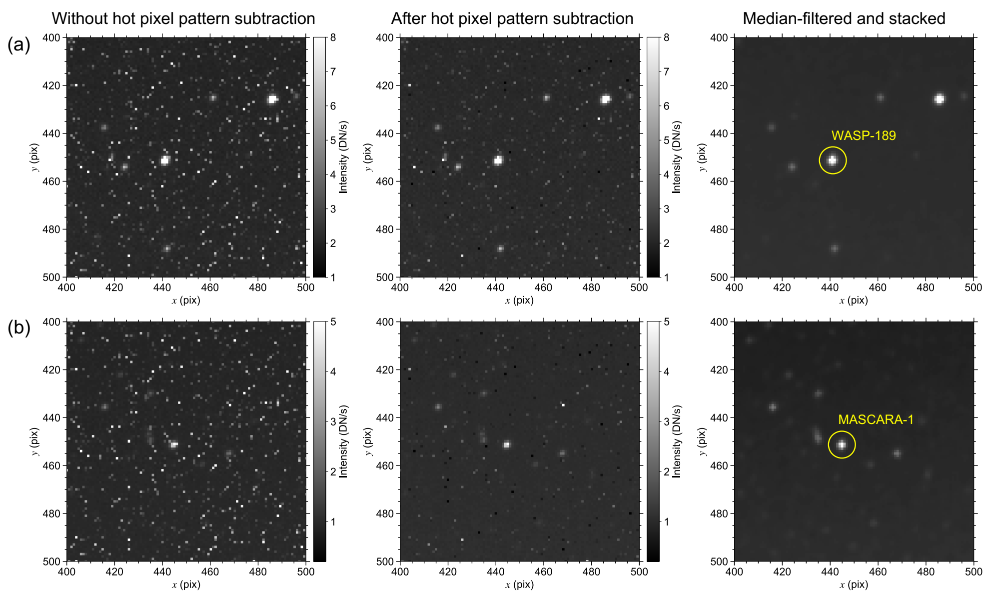

Figure 2. ONC-T images of **(a)** WASP-189 (image hyb2_onc_20240918_073620_tif_l2b) and **(b)** MASCARA-1 (image hyb2_onc_20241130_093826_tif_l2b) captured during transit events 10 and 12, respectively. The left panels show a single reduced ONC-T image ($p^t(x, y)$) without hot pixel correction (i.e., data reduced assuming $p_{\rm hot} = 0$ in Equation 1). The center panels show the same reduced images with hot pixel subtraction. The right panels show the reduced ONC-T image after applying a 3 × 3-pixel median filter and stacking all frames co-aligned on the target star, allowing the stellar positions to be clearly visualized. The host stars are marked with circles.

(S. Kameda et al. 2021). The terms $p_{\rm bias}$ and $p_{\rm dark}$ denote the bias and dark current intensities, respectively, and $p_{\rm hot}$ is the hot pixel pattern. These terms depend on $T_{\rm CCD}$, $T_{\rm ELE}$, and $T_{\rm AE}$, which are the temperatures of the CCD detector, sensor head electronics, and analogue electronics control unit, respectively; see E. Tatsumi et al. (2019) for the functional forms of $p_{\rm bias}$ and $p_{\rm dark}$. Although hot pixel correction has not been included in the nominal data reduction procedure of ONC-T, the significant increase in hot pixels over time, with some reaching intensities comparable to that of the host star, motivated their correction. The hot-pixel patterns were derived by calculating the pixel-wise minimum of two deep-space images acquired at different spacecraft pointings. The reduced images with and without hot pixel correction are compared in Fig. 2. After correction, the amplitudes of the hot pixels were greatly reduced, remaining well below the level of the stellar signal. In addition, none of the stars in the images were saturated, ensuring that blooming from nearby bright sources did not compromise the photometric analysis.

The light curve (I^t) was obtained using aperture photometry:

$$I^t = \sum_{(x,y)\in S_{\rm star}} p^t(x,y) \; - \sum_{(x,y)\in S_{\rm bg}} p^t(x,y). \qquad (2)$$

Here, $S_{\rm star}$ denotes the set of pixel coordinates within the circular aperture used to measure the stellar signal, and $S_{\rm bg}$ refers to those within the surrounding annulus for background estimation; both are centered on the stellar centroid. The aperture and annulus sizes were optimized to minimize the RMS of the residuals with respect to the model described in Section 3.2. Integration was performed over the precise intersection of these regions with each pixel using the `photutils` library. To mitigate the effects of cosmic rays, a 3σ clipping algorithm was applied during background estimation. In addition, data points deviating by more than three times the interquartile range of I^t within a one-hour sliding window were removed.

Since the stellar position drifted over the course of the observations, the centroid was recalculated in each image using a 2D Gaussian fit. In most cases, the star drifted a few pixels in the $-x$ direction during the first five hours and then stabilized to within ∼1 pixel (Fig. 3a). In Event 14, a sudden jump occurred about one hour into the observation. These positional shifts are attributed to spacecraft pointing instability, as the attitude was adjusted from nominal to the target orientation only 1–2 hours before observations.

A similar drift was observed in the CCD temperature (Fig. 3b). Although the heater was set to maintain the CCD between −30 and −28°C, the temperature typically rose during the first ∼8 hours of each observation, reaching as high as −23°C in the most extreme case before asymptotically stabilizing.

For the I^t of TESS data, we used the Pre-search Data Conditioning Simple Aperture Photometry (PDCSAP) flux, provided at a 120-second cadence and processed by the TESS Science Processing Operations Center at NASA Ames Research Center (J. M. Jenkins et al. 2016). For each transit event, data were extracted within a 26-hour window centered on the predicted mid-transit time, although coverage within this window was not always continuous. Data points flagged with quality values of 1, 2, 4, 8, 32, or 128 were excluded (J. D. Twicken et al. 2020).

3.2. *Transit modeling and noise decorrelation*

For each transit event, the light curve I^t was normalized by its median to obtain $\widehat{I}^t$, and then fit with a model combining the transit signal ($\mathcal{T}(t)$) and a systematic noise component ($\mathcal{N}(t)$):

$$\widehat{I}^t = \mathcal{T}(t) + \mathcal{N}(t). \qquad (3)$$

For $\mathcal{T}(t)$, we used the K. Mandel & E. Agol (2002) transit model as implemented in the `PyTransit` library (H. Parviainen 2015), assuming a circular orbit and a quadratic limb-darkening law. The out-of-transit baseline of $\mathcal{T}(t)$ equals one. Following the approach used in previous TTV studies (e.g., A. Kokori et al. 2022; E. S. Ivshina & J. N. Winn 2022), we fitted the mid-transit time (T_C) and the planet-to-star radius ratio (R_p/R_*), while fixing the orbital period (P), semi-major-axis–to–star-radius ratio (a/R_*), orbital inclination (i_p), and quadratic limb-darkening coefficients (u_1, u_2) to literature values: P =2.7240308 days (E. S. Ivshina & J. N. Winn 2022), a/R_*=4.6, i_p=84.03°, u_1=0.495, u_2=0.055 (M. Lendl et al. 2020) for WASP-189 b and P =2.14877381 days, a/R_*=4.1676, i_p=88.45°, u_1=0.392, u_2=0.092 (M. J. Hooton et al. 2022) for MASCARA-1 b. Since the fitting was performed individually for each transit event, the assumed orbital period influences the fit only through its effect on the transit duration, not on the mid-transit time. A precise value of the orbital period is later derived from the compiled set of T_C (Section 4.2).

For the ONC-T data, pixel-level decorrelation (PLD) model was used as $\mathcal{N}(t)$ to account for spacecraft pointing instabilities:

$$\mathcal{N}(t) = \sum_{(x_i,y_i)\in M} c(x_i,y_i)\,\frac{p^t(x_i,y_i)}{\sum\limits_{(x_j,y_j)\in M} p^t(x_j,y_j)} + \alpha + \beta\,(t-t_0) + \eta\left[1-\exp\!\left(-\tfrac{t-t_0}{\tau}\right)\right]. \qquad (4)$$

The first term represents the first-order PLD model (D. Deming et al. 2015), while the remaining terms account for time-correlated noise. The set of pixel coordinates used as the PLD basis vector is denoted by M, and each of their coefficients are denoted by c. The time-correlated component is modeled as a combination of a linear trend and an exponentially decaying function that asymptotically approaches zero. Here, t_0 denotes the start time of observation. The decaying function is intended to model noise correlated with CCD temperature, which follows a similar temporal pattern (Fig. 3b). The fitting parameters are $c(x_i, y_i)$ for $i = 1, 2, \ldots, |M|$, as well as α, β, η, and τ. For the PLD basis vectors, we selected pixels within a 3 × 3 window centered on the mean stellar centroid, supplemented by any additional pixels the centroid crossed in individual frames. This resulted in a total of $|M| = 9$ to 15 pixels, depending on the degree of pointing stability. This selection strategy

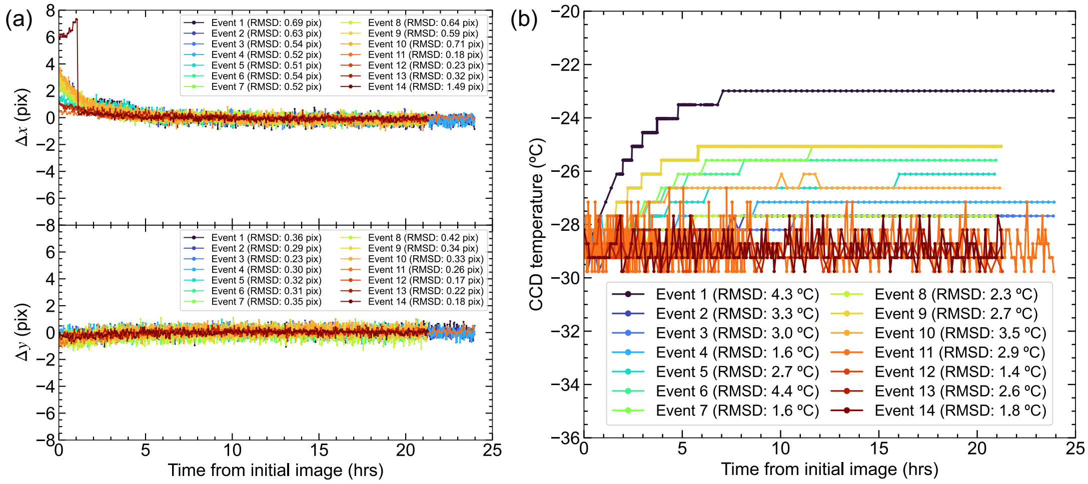

Figure 3. Pointing and temperature stability of ONC-T during each transit observation. **(a)** The top and bottom panels show the horizontal (x) and vertical (y) centroid positions of the host star, respectively, expressed as deviations from their median values. **(b)** CCD temperature measured during each observation. The temperature readings are quantized in steps of 0.52°C. The root mean square deviation (RMSD) from the median is indicated in the legend of each panel.

effectively enabled the PLD model to capture pointing drift during the initial phase of the observation, while avoiding an excessive increase in the number of model parameters.

For the TESS data, a third order polynomial was used as $\mathcal{N}(t)$:

$$\mathcal{N}(t) = \alpha \ + \ \beta(t - t_0) \ + \ \gamma(t - t_0)^2 \ + \ \delta(t - t_0)^3. \quad (5)$$

Here, the coefficients α, β, γ, and δ are the fitting parameters.

The parameter spaces of both $\mathcal{T}(t)$ and $\mathcal{N}(t)$ were jointly explored using the Markov Chain Monte Carlo (MCMC) sampling implemented in the `emcee` library (D. Foreman-Mackey et al. 2013). We adopted uniform priors for all parameters and ran the MCMC with 1,024 walkers for 10,000 steps, discarding the first 5,000 as burn-in. The best-fit parameter values and their 1σ credible intervals were obtained as the median and standard deviation of the marginalized posterior distributions, respectively.

3.3. *Blind search of the exoplanet using Transit Least Squares*

While the modeling described in Section 3.2 assumes the presence of a transit signal, we also applied an alternative approach that makes no such assumption to test whether the transit signal can be recovered solely from ONC-T data. In this approach, we set $\mathcal{T}(t) = 1$ (no transit model) and fit the data using only $\mathcal{N}(t)$.

A periodic transit signal was searched for in the noise-detrended light curves ($\widehat{I}^t - \mathcal{N}(t)$) of all events using the Transit Least Squares (TLS) algorithm implemented in the `transitleastsquares` library (M. Hippke & R. Heller 2019). TLS has been widely used to find transit signals in Kepler and TESS data (e.g., V. Van Grootel et al. 2021; J. Lillo-Box et al. 2020). The method phase-folds the light curve over a range of trial periods and computes the signal detection efficiency (SDE), which quantifies the statistical significance of a transit at each trial period. The false-positive rate of transit detections drops below 1% when the SDE exceeds 7.

4. RESULTS: SUCCESSFUL TRANSIT DETECTIONS BY ONC-T

4.1. *Statistics of transit light curves observed by ONC-T*

The ONC-T data reveal statistically significant transit signals from both WASP-189 b and MASCARA-1 b. The raw light curve ($\widehat{I}^t$; Fig. 4 left) exhibits a rising baseline during the first ~8 hours, likely due to drifts in CCD temperature and spacecraft pointing (Fig. 3). Despite this, the transit dip extending approximately ±2 hours from mid-transit is clearly visible. After subtracting the systematic noise ($\widehat{I}^t - \mathcal{N}(t)$; Fig. 4 center), the baseline flattens, making the transit more distinct. The photometric precision per ONC-T image is calculated as $0.46 \pm 0.05\%$ for WASP-189 b and $0.65 \pm 0.06\%$ for MASCARA-1 b, based on the RMS of the residuals: $\widehat{I}^t - [\mathcal{T}(t) + \mathcal{N}(t)]$ (Fig. 4 right). We assess the significance of the transit signal by calculating its SNR using the following equation:

$$\text{Transit SNR} \ = \ \frac{T_{\text{dep}}}{\sqrt{\sigma_{\text{in}}^2 + \sigma_{\text{out}}^2}}. \quad (6)$$

Here, T_{dep} is the transit depth, σ_{in} is the standard error of the in-transit flux, and σ_{out} is the standard error of

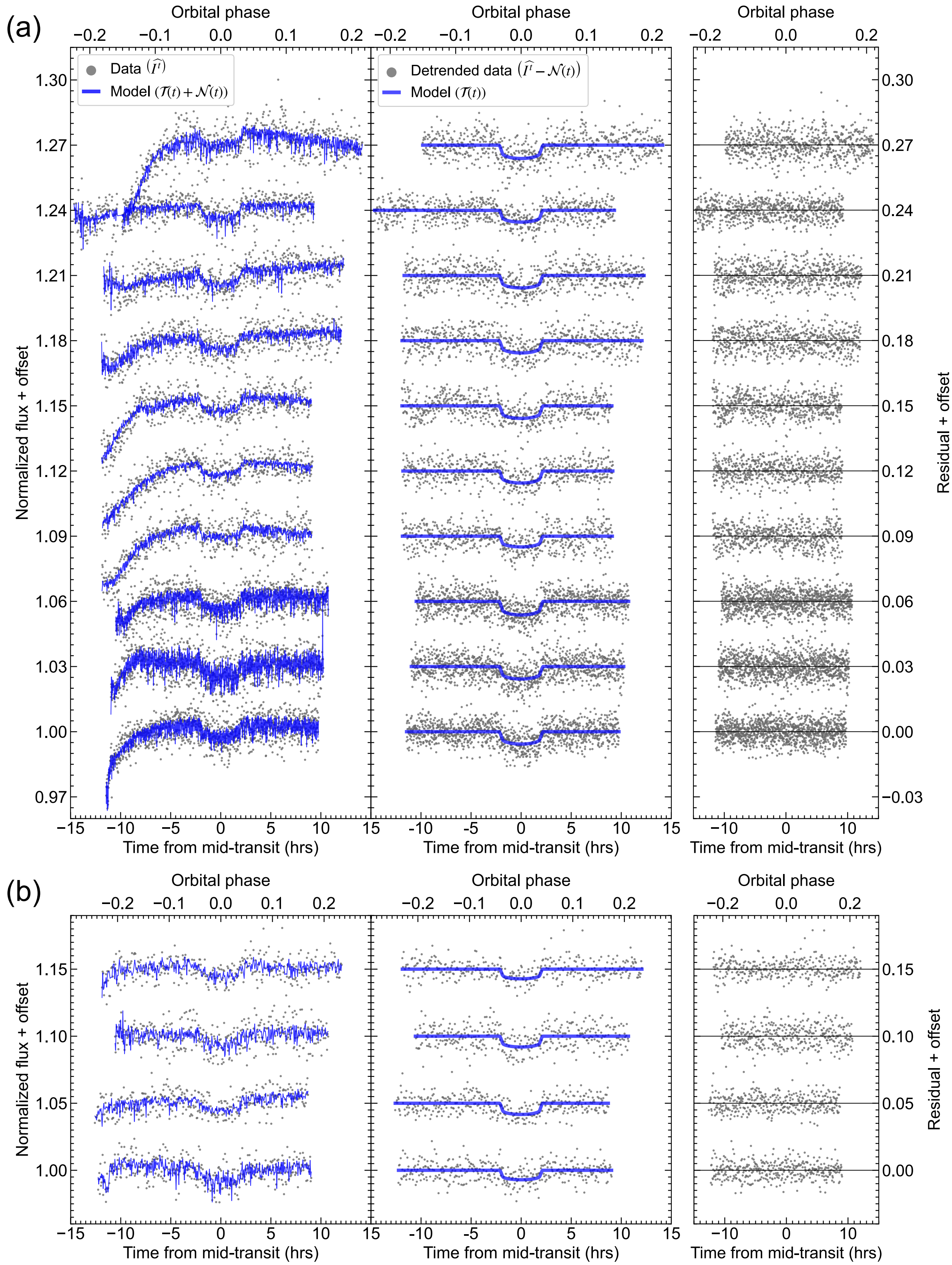

Figure 4. Light curves for each transit of **(a)** WASP-189 b and **(b)** MASCARA-1 b observed by ONC-T. Left panels show the raw light curves ($\widehat{I^t}$), with blue curves representing the combined transit and noise model fit ($\mathcal{T}(t) + \mathcal{N}(t)$). Center panels display the noise-detrended light curves ($\widehat{I^t} - \mathcal{N}(t)$), with blue curves showing the fitted transit model ($\mathcal{T}(t)$). Right panels show the residuals: $\widehat{I^t} - [\mathcal{T}(t) + \mathcal{N}(t)]$. Light curves from transit events 1–10 for WASP-189 b and 11–14 for MASCARA-1 b are displayed from top to bottom in each panel. Each light curve is vertically offset for clarity by 0.03 in panel (a) and 0.05 in panel (b).

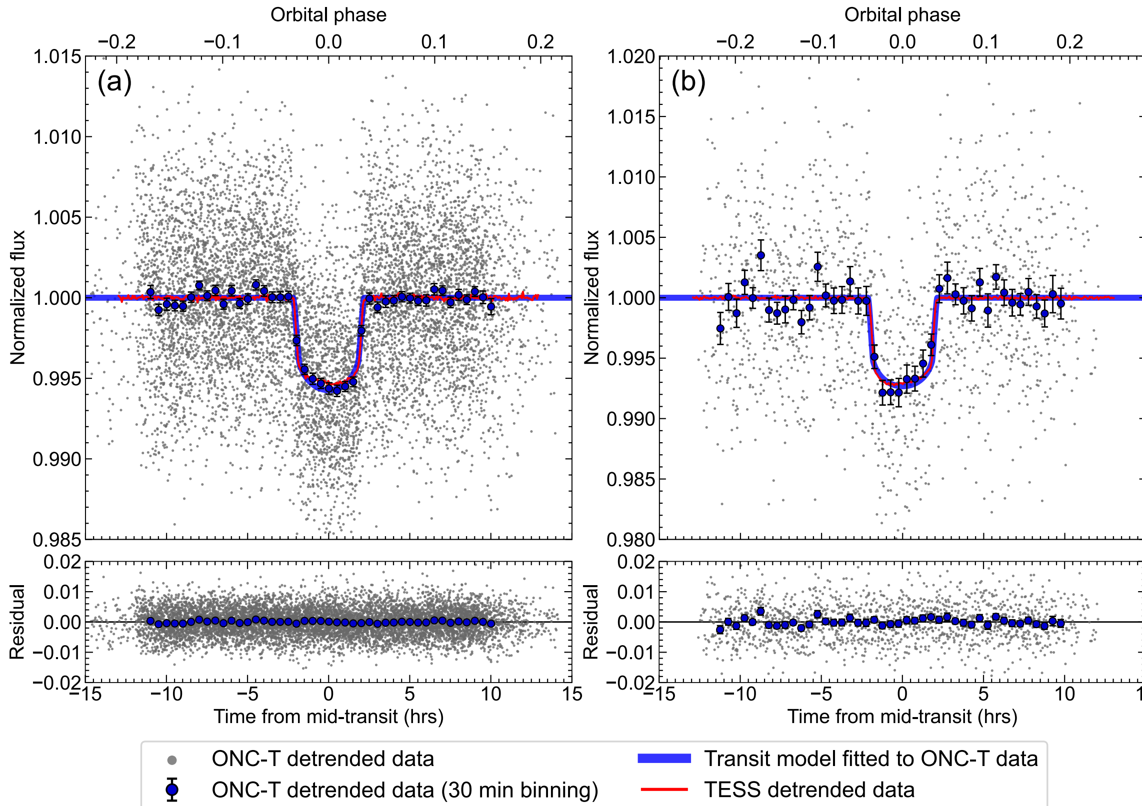

Figure 5. Phase-folded light curves of **(a)** WASP-189 b and **(b)** MASCARA-1 b from ONC-T and TESS data. The top panels show the phase-folded detrended light curves ($\widehat{I}^t - \mathcal{N}(t)$), while the bottom panels display the residuals of the ONC-T data relative to the fitted transit model ($\mathcal{T}(t)$; solid blue curve). Gray points show the flux measured in individual ONC-T images, while blue circles represent 30-minute binned averages, with error bars indicating the standard error. Error bars are not visible when smaller than the marker size. The red curve represents the TESS light curve, baseline-corrected and binned over 4-minute intervals.

Table 3. Updated reference epoch (T_0) and orbital period (P) compared with values reported in the latest literature.

	T_0 ($\mathrm{BJD_{TDB}}$)	P (days)
WASP-189 b		
Updated (This study)	$2456706.456164 \pm 0.000313$	$2.72403141 \pm 0.00000035$
Literature (E. S. Ivshina & J. N. Winn 2022)	$2456706.456600 \pm 0.002300$	$2.72403080 \pm 0.00000280$
MASCARA-1 b		
Updated (This study)	$2458833.488125 \pm 0.000079$	$2.14876998 \pm 0.00000013$
Literature (M. J. Hooton et al. 2022)	$2458833.488151^{+0.000091}_{-0.000092}$	$2.14877381^{+0.00000088}_{-0.00000087}$

the out-of-transit flux. The transit SNR evaluated for a single transit event is 12.5 ± 2.7 for WASP-189 b and 7.9 ± 0.7 for MASCARA-1 b.

After phase folding the 10 transit observations of WASP-189 b and four of MASCARA-1 b, their transit SNR increase to 39.8 and 15.6, respectively (Fig. 5). The shapes of the phase-folded light curves closely resemble those observed by TESS. The TESS data exhibit asymmetric transit curves, attributed to gravity darkening induced by the host star's rapid rotation (M. Lendl et al. 2020; M. J. Hooton et al. 2022). A similar asymmetry is visible in the ONC-T data, although its magnitude is comparable to the uncertainty.

The posterior distributions of the derived T_C and R_p/R_* follow unimodal Gaussian shapes and show negligible mutual correlation (correlation coefficient < 0.04; Appendix A). The 1σ precision in T_C derived from a single transit is 5.4 min for WASP-189 b and 6.9 min for MASCARA-1 b. The 1σ precision in R_p/R_* is 0.0036 (5.1% relative) for WASP-189 b and 0.0062 (7.7% relative) for MASCARA-1 b. A higher precision was achieved in events 8–10 of WASP-189 b, owing to a roughly twofold reduction in the imaging cadence by minimizing overhead duration (Table 2).

4.2. *Transit timing analyses*

We fit the following linear ephemeris model, assuming a constant orbital period, to all T_C values derived from ONC-T, TESS, and previous observations:

$$T_C(N) = T_0 + NP. \tag{7}$$

Here, N is the orbit number and T_0 is the reference epoch at $N = 0$. Using this model, we generate an O – C diagram (Fig. 6a) that shows the deviation of the observed T_C values from those computed by the fitted linear ephemeris. We also test to fit the data with a quadratic ephemeris model that accounts for a constant change in orbital period due to orbital decay (K. C. Patra et al. 2017):

$$T_C(N) = T_0 + NP + \frac{1}{2}\frac{dP}{dN}N^2. \tag{8}$$

Here, dP/dN represents the orbital decay rate. The model parameters and their uncertainties are derived using MCMC with uniform priors, following the same procedure described in Section 3.2.

The T_C derived from ONC-T data show no systematic deviation from the fitted linear ephemeris model (Fig. 6a). The average O – C values are –1.2 min for WASP-189 b and +2.1 min for MASCARA-1 b, indicating that measurement accuracy of T_C is better than ∼2 min.

The new transit data from TESS and ONC-T enabled us to refine the ephemeris models (Table 3). For WASP-189 b, the uncertainties in T_0 and P were reduced by a factor of ∼6, while remaining consistent with the values reported by E. S. Ivshina & J. N. Winn (2022) within their uncertainties. All reported transit timings show no significant deviation from the linear ephemeris model. The orbital decay rate dP/dN derived from the quadratic model is $-1.8 \pm 4.7 \times 10^{-9}$ days, indicating no significant change in the orbital period over the past 10.6 years, from Feb 2014 to Sep 2024.

In contrast, for MASCARA-1 b, we find a significant discrepancy of 4σ between our refined ephemeris model and those reported in the literature (M. J. Hooton et al. 2022; Table 3). M. J. Hooton et al. (2022) derived the orbital period based on observations of three transits (two from CHEOPS and one from Spitzer/IRAC at 4.5 µm) and four occultations (two each from CHEOPS and Spitzer). This ephemeris aligns better with earlier transit timings reported by G. J. J. Talens et al. (2017), but deviates significantly from recent TESS observations by up to 4.4 ± 0.4 min. Conversely, the ephemeris model derived in this study is consistent with recent TESS data, yet shows a discrepancy of 6 ± 3 min with the G. J. J. Talens et al. (2017) timings. Including an orbital decay term does not resolve this discrepancy; the derived dP/dN of $-4.1 \pm 9.6 \times 10^{-10}$ days indicates no constant change in the orbital period. The cause of this discrepancy may require further investigation through continued monitoring of transit timings and by considering models that account for other sources of TTVs. The ONC-T data acquired to date are consistent with both the refined and literature ephemerides within the errors. Nevertheless, ONC-T is expected to distinguish between the two models with 2σ significance by 2030, during which Hayabusa2 is planned to still be in cruise. We recommend using the updated ephemeris derived in this study for planning future transit observations, as it provides a better match to recent data.

4.3. *Transit depth analyses*

The R_p/R_* values derived from ONC-T data agree with those from TESS data within 0.0011 (1.6% relative) for WASP-189 b and 0.0025 (3.1% relative) for MASCARA-1 b, supporting that the ONC-T measurements are accurate to at least these levels (Fig. 6b).

The R_p/R_* values derived from recent ONC-T and TESS observations are generally consistent with past measurements, showing no significant changes over time. The relatively low R_p/R_* of WASP-189 b reported by D. R. Anderson et al. (2018) has been attributed to potential inaccuracies due to the lack of full ingress-

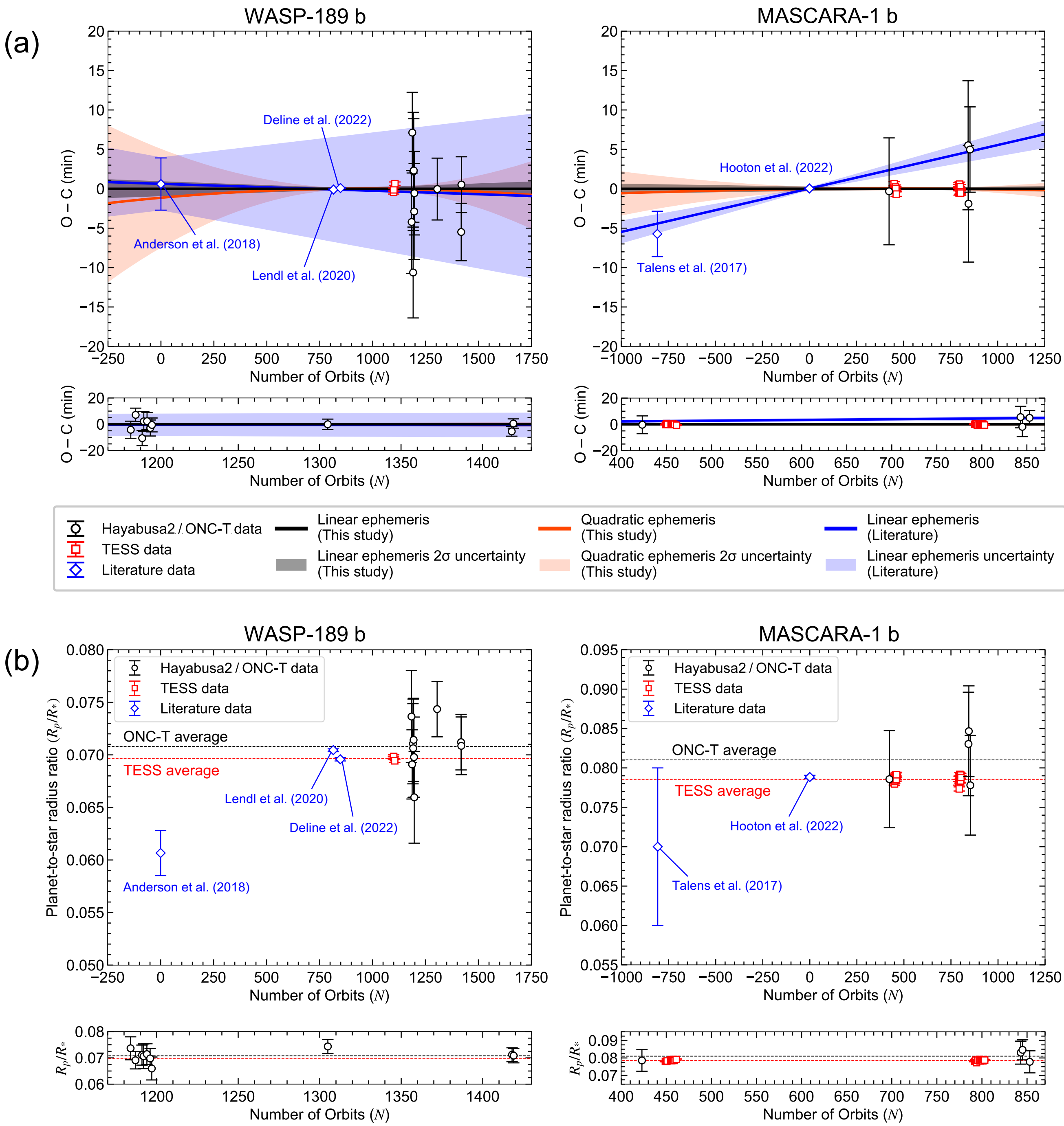

Figure 6. **(a)** Transit timing and **(b)** planet-to-star radius ratio (R_p/R_*) variations of **(left)** WASP-189 b and **(right)** MASCARA-1 b. The O – C values on the vertical axis in (a) represent the difference between the observed transit times and those computed by the linear ephemeris model derived in this study. The fitted linear and quadratic models are shown as black and red lines, respectively, with their 2σ uncertainty regions indicated by hatching. For comparison, the linear model reported in the most recent literature is shown in blue, with its reported uncertainty shaded. For each figure in (a) and (b), the bottom panels provide a magnified view of the ONC-T observation period. Data points from the literature are labeled with their respective references.

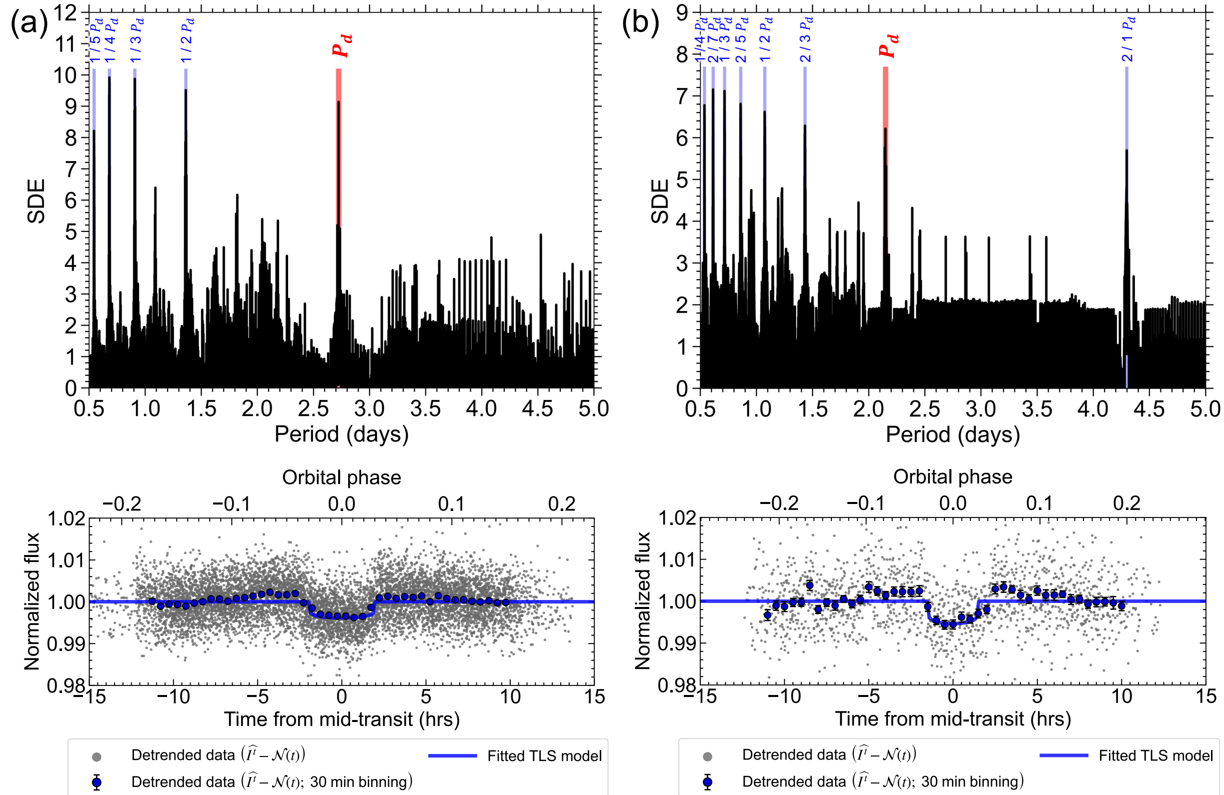

Figure 7. TLS analysis results for **(a)** WASP-189 b and **(b)** MASCARA-1 b. The top panels show the TLS periodograms, with the red vertical line marking the detected period (P_d), consistent with the true orbital period (P). Blue lines indicate additional peaks with SDE > 6 for WASP-189 b and SDE > 4 for MASCARA-1 b; all correspond to rational multiples or fractions of P_d. The bottom panels display the detrended light curves ($\widehat{I}^t - \mathcal{N}(t)$) phase-folded at P_d. Gray points show the flux measured in individual ONC-T images, while blue circles represent 30-minute binned averages, with error bars indicating the standard error. Error bars are not visible when smaller than the marker size. The solid blue curve is the best-fit TLS model.

to-egress coverage in their follow-up observations and the scarcity of nearby reference stars (M. Lendl et al. 2020). Our results further support this interpretation. For MASCARA-1 b, G. J. J. Talens et al. (2017) reported large uncertainties in R_p/R_*, caused by discrepancies between measurements from the MASCARA and NITES telescopes: $R_p/R_* = 0.063^{+0.002}_{-0.001}$ from MASCARA data and $0.078^{+0.002}_{-0.001}$ from NITES data. Our results align with the NITES-based estimate.

4.4. *Transit Least Squares analyses*

The TLS analysis demonstrates successful true-positive detections of the exoplanets, indicating that ONC-T data alone provide sufficient information for their detection. The TLS periodograms (Fig. 7) show a significant peak near the actual orbital periods of the exoplanets. The period of the detected peak (P_d) is 2.72392 ± 0.00048 days for WASP-189 b and 2.14877 ± 0.00031 days for MASCARA-1, where the uncertainties correspond to the half-width at half-maximum. These periods are consistent with the actual orbital periods within their errors (Table 3). The SDE at P_d is 9.1 for WASP-189 b and 6.2 for MASCARA-1 b. The SDE for WASP-189 b exceeds the commonly adopted threshold of 7, corresponding to a false-positive rate below 1% (M. Hippke & R. Heller 2019). Although the SDE for MASCARA-1 b falls below this threshold, likely due to its fainter host star and fewer observed transits, it can still be considered a strong planetary candidate, as some studies adopt an empirical threshold of SDE > 6 (e.g., C. D. Dressing & D. Charbonneau 2015).

All other peaks with SDE values comparable to that at P_d correspond to rational multiples or fractions of P_d. This pattern arises from aliasing effects due to the non-continuous temporal coverage of ONC-T observations. Therefore, even peaks with higher SDEs than at P_d do not necessarily indicate false positives. Although the risk of false-positive detections cannot be entirely ruled out, since the observation windows were intentionally aligned with the expected transit times, the flat out-of-transit flux profile suggests that false positives are unlikely to be a significant concern.

In addition, the TLS analysis confirms that $\mathcal{N}(t)$ does not overfit the transit signal. When $\mathcal{T}(t)$ is omitted and the data are fitted using only $\mathcal{N}(t)$, the resulting light curves exhibit a slightly wing-shaped baseline (Fig. 7, bottom), in contrast to the cleaner baselines obtained when $\mathcal{T}(t)$ is included (Fig. 5). Nevertheless, the transit shape is well preserved, supporting the reliability of our denoising approach.

5. DISCUSSION: IMPLICATIONS FOR FUTURE SMALL SATELLITE OBSERVATIONS

Building on the benchmark established by ONC-T, we derive a formula to estimate the transit detectability by future missions. Assuming photon shot noise is the dominant noise source, the transit SNR (Equation 6) can be estimated for a wide range of targets and instrument parameters using the following formula (A. Kokori et al. 2022, 2023):

$$\text{Predicted SNR} =$$
$$Q \cdot D \cdot T_{\text{dep}} \cdot \sqrt{10^{-m/2.5}} \left(\frac{1}{T_{\text{dur}}} + \frac{1}{T - T_{\text{dur}}} \right)^{-\frac{1}{2}} . \quad (9)$$

Here, D is the aperture diameter in millimeters, m is the apparent magnitude of the host star at the observed wavelength, T_{dep} is the transit depth in percent, T_{dur} is the transit duration in hours, and T is the total observation time in hours. The scaling factor Q is an empirical constant derived from ONC-T observations. We find $Q = 20.88$, under which the predicted transit SNR for MASCARA-1 b ($m = 8.3$, $T_{\text{dep}} = 0.62\%$, and $T_{\text{dur}} = 4.2$ hours) matches the observed SNR of 7.9 under ONC-T's observation conditions ($D = 15$ mm; $T = 21$ hours). Based on the empirical relation between the transit SNR and SDE found in this study, a transit SNR above $\sim$10 is likely required to achieve SDE > 7 and confidently detect a new exoplanet.

We confirm that Equation 9 predicts transit SNRs with reasonable accuracy. For instance, the formula predicts a transit SNR of 15.0 for WASP-189 b observed by ONC-T, in good agreement with the observed SNR (Section 4.1). For the TESS observations, the predicted SNRs are 105 for WASP-189 b and 55 for MASCARA-1 b, both consistent with the observed values of 130 and 70, respectively, within 30%. The slight underestimation likely results from ONC-T's lower pointing and thermal stability compared to TESS (Table 1), along with longer overhead durations. For 55 Cnc e observed by ASTERIA, the predicted SNR of 3.8 agrees within a factor of two with the observed SNR of 2.2 (M. Knapp et al. 2020). The observed SNR is lower in this case likely due to contamination from the nearby star 53 Cnc or increased pixel-to-pixel gain variations inherent to ASTERIA's CMOS design.

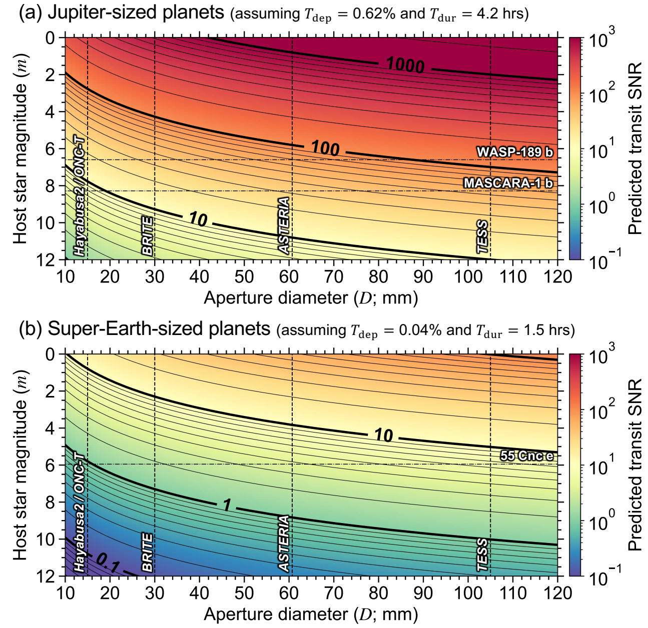

Figure 8. Predicted transit signal-to-noise ratio (SNR) for **(a)** Jupiter-sized and **(b)** super-Earth-sized planets, shown as a function of telescope aperture diameter (x-axis) and host star magnitude (y-axis). Vertical dashed lines indicate the apertures of past space-based instruments. Horizontal lines mark the host star magnitudes of WASP-189 b and MASCARA-1 b in panel (a), and 55 Cnc e in panel (b). For the Jupiter-sized planet case, the transit depth (T_{dep}) and duration (T_{dur}) of MASCARA-1 b were assumed in the SNR prediction. For the super-Earth-sized planet case, the corresponding values of 55 Cnc e were used.

We use Equation 9 to estimate transit SNRs across a range of D and m conditions (Fig. 8). For instruments with aperture sizes as small as that of ONC-T, the predicted SNR of Jupiter-sized planets exceeds 10 when the host star is brighter than $m \sim 7.5$. More than 25,000 stars across the sky surpass this brightness threshold (E. Høg et al. 2000). Assuming each of these stars hosts a single Jupiter-sized planet with an orbital period uniformly distributed in $\log_{10}$(Period) from 1 day to 100 years, we estimate that approximately 40, 15, and 3 transiting Jupiters would be detectable for orbital periods longer than 100 days, 1 year, and 10 years, respectively [11]. Thus, our results suggest that long-term pho-

[11] We assume the geometric transit probability $(R_* + R_p)/a$ to be

$$\frac{R_\odot + R_J}{1\,\text{AU}} \left(\frac{P}{365\,\text{days}} \right)^{-2/3},$$

where $R_\odot$ and R_J are the solar and Jovian radii, respectively, expressed in astronomical units (AU). This expression assumes a circular orbit, a host star with solar mass and radius, and a planet with Jupiter's radius.

tometric monitoring of bright stars using small satellites equipped with ONC-T-class optics could play a valuable role in surveying the population of long-period (>100 days) transiting planets, which remain underrepresented in current surveys (Fig. 1b). In contrast, detecting super-Earth-sized planets with similar instrumentation requires much brighter host stars. For ONC-T-class optics, achieving an SNR greater than 10 is only possible for stars brighter than about $m \sim 1$, of which there are only around 10. This suggests that larger apertures are necessary to gather statistically meaningful data on super-Earth populations. For instance, increasing the aperture to 60 mm would raise the brightness threshold to $m \sim 4$ and expand the number of stars to over 500.

6. CONCLUSIONS

We reported the successful transit detections of two known hot Jupiters, WASP-189 b and MASCARA-1 b, using the telescopic Optical Navigation Camera (ONC-T) onboard the Hayabusa2 spacecraft. With its effective aperture diameter of 15 mm, ONC-T sets a new record for the smallest aperture optics to detect an exoplanet transit from space. Each transit event of WASP-189 b and MASCARA-1 b were detected with signal-to-noise ratios (SNR) of 13 and 8, respectively. Combining all observed transits (ten for WASP-189 b, four for MASCARA-1 b) increased the SNR to 40 and 16. A blind search for transit signals using the Transit Least Squares (TLS) algorithm successfully recovered periodic signals with signal detection efficiencies (SDEs) exceeding 9 for WASP-189 b and 6 for MASCARA-1 b.

Transit mid-times (T_C) for WASP-189 b and MASCARA-1 b were measured with precisions of 5 and 7 minutes, respectively, per single transit. Their planet-to-star radius ratios (R_p/R_*) were measured with precisions of 0.004 (5% relative) and 0.006 (8% relative), respectively, per transit. The T_C and R_p/R_* derived from ONC-T data agree with those from TESS within accuracies better than 2 minutes and 0.002 (3% relative), respectively. Combining all T_C data from ONC-T, TESS, and literatures, we reduced the uncertainties in the ephemerides of both planets. Notably, the updated orbital period of MASCARA-1 b (2.14876998 $\pm$ 0.00000013 days) differs from previous literature by 4σ, suggesting possible transit timing variations and highlighting the need for continued monitoring.

The successful transit detections and characterizations by ONC-T demonstrate that compact optics, such as those deployable on CubeSats and nanosatellites, can play a significant role in advancing exoplanet population studies. Using ONC-T as a benchmark, we developed a formula to predict transit SNR across various target brightnesses and aperture sizes. One promising application of optics as small as ONC-T's is the search for transiting, long-period (>100 days) Jupiter-sized planets—a population still underrepresented in current catalogs—through long-term monitoring of stars brighter than approximately magnitude 7.5.

7. DATA

All the *TESS* data used in this paper can be found in MAST: 10.17909/t9-nmc8-f686. Data presented in Fig. 1 can be found in the NASA Exoplanet Archive: 10.26133/NEA1.

ACKNOWLEDGEMENTS

We are grateful to the Hayabusa2 team for their years of dedicated operations and for making the exoplanet observations possible. We deeply appreciate Dr. Rie Honda's commitment to the development, data archiving, and operations of the Optical Navigation Camera onboard Hayabusa2. This work was supported by Grant-in-Aid for JSPS Fellows Grant number 24KJ2228.

AUTHOR CONTRIBUTIONS

KY led the observation planning, data analysis, and manuscript preparation. ONC-T operations were conducted by KY, MY, TM, YC, YY, MH, ET, MM, NS, SK, ST, and SSu, under the supervision of TK. YM and SSh managed the planning of spacecraft attitude during the observations. KE and AA provided valuable feedback and contributed to improving the manuscript.

APPENDIX

A. POSTERIOR DISTRIBUTIONS OF T_C AND R_P/R_*

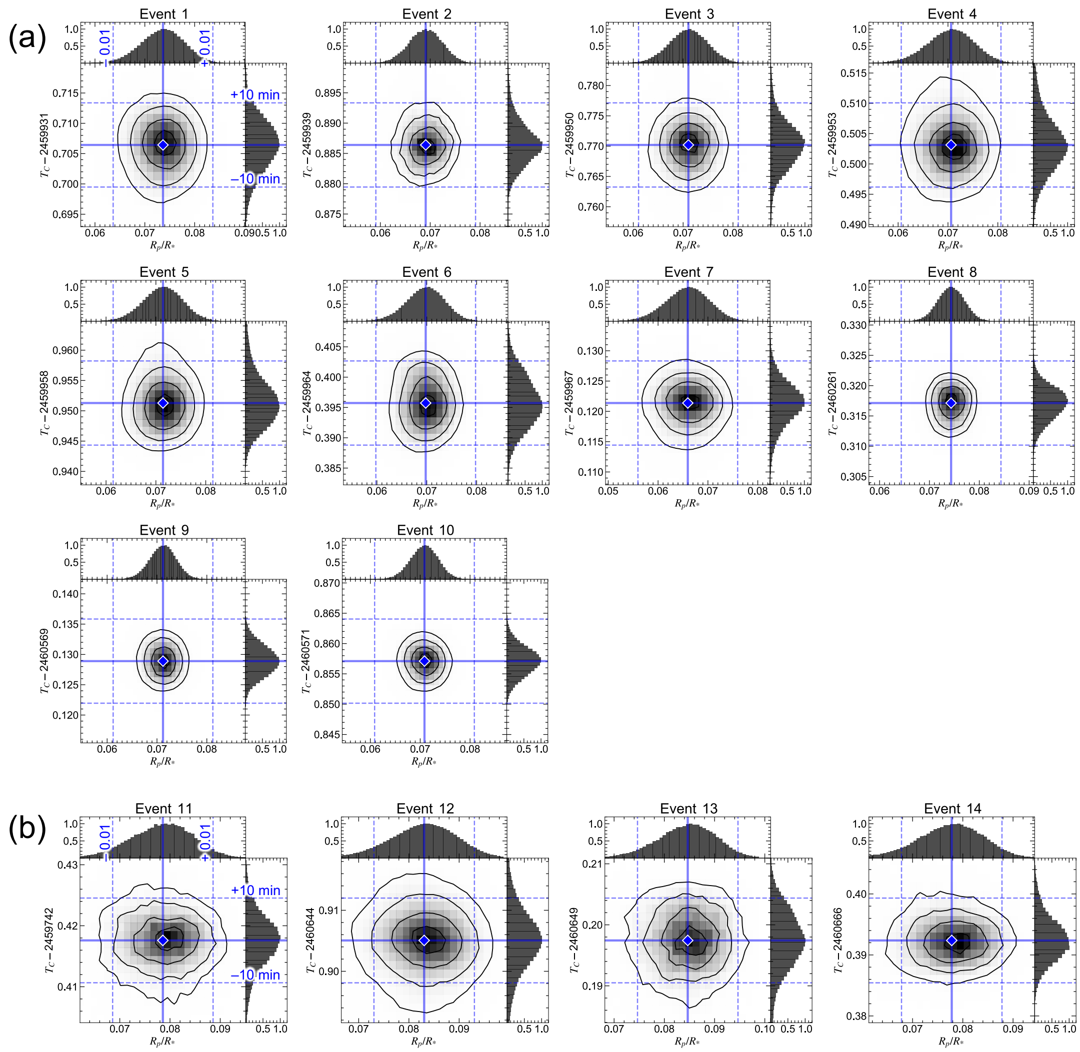

Figure 9. Posterior distributions of transit mid-times (T_C) and planet-to-star radius ratios (R_p/R_*) for each transit of **(a)** WASP-189 b (Event 1–10) and **(b)** MASCARA-1 b (Event 11–14) observed by ONC-T. The 2D histograms show the covariance between R_p/R_* and T_C, with contours marking the 0.5σ, 1σ, 1.5σ, and 2σ confidence levels. The top and right panels display marginal histograms. Blue markers and crosshairs indicate the medians values, while blue dashed lines mark $\pm$0.01 and $\pm$10-minute intervals from the medians of R_p/R_* and T_C, respectively.

REFERENCES

Ananyeva, V. I., Ivanova, A. E., Shashkova, I. A., et al. 2022, Astronomy Reports, 66, 886, doi: 10.1134/S106377292210002X

Anderson, D. R., Temple, L. Y., Nielsen, L. D., et al. 2018, arXiv e-prints, arXiv:1809.04897, doi: 10.48550/arXiv.1809.04897

Chaturvedi, P., Deshpande, R., Dixit, V., et al. 2014, MNRAS, 442, 3737, doi: 10.1093/mnras/stu1127

Cumming, A., Butler, R. P., Marcy, G. W., et al. 2008, PASP, 120, 531, doi: 10.1086/588487

Deming, D., Knutson, H., Kammer, J., et al. 2015, ApJ, 805, 132, doi: 10.1088/0004-637X/805/2/132

Dressing, C. D., & Charbonneau, D. 2015, ApJ, 807, 45, doi: 10.1088/0004-637X/807/1/45

Egan, A., Nell, N., Suresh, A., et al. 2023, AJ, 165, 64, doi: 10.3847/1538-3881/aca8a3

Eyles, C. J., Harrison, R. A., Davis, C. J., et al. 2009, SoPh, 254, 387, doi: 10.1007/s11207-008-9299-0

Foreman-Mackey, D., Hogg, D. W., Lang, D., & Goodman, J. 2013, PASP, 125, 306, doi: 10.1086/670067

Foreman-Mackey, D., Morton, T. D., Hogg, D. W., Agol, E., & Schölkopf, B. 2016, AJ, 152, 206, doi: 10.3847/0004-6256/152/6/206

France, K., Fleming, B., Egan, A., et al. 2023, AJ, 165, 63, doi: 10.3847/1538-3881/aca8a2

Fuentes, A., & Solar, M. 2024, Astronomy and Computing, 47, 100816, doi: 10.1016/j.ascom.2024.100816

Grocott, S., Zee, R., & Matthews, J. 2004, in Proceedings of the Small Satellite Conference (SmallSat) 2004. https://digitalcommons.usu.edu/smallsat/2004/All2004/50/

Hippke, M., & Heller, R. 2019, A&A, 623, A39, doi: 10.1051/0004-6361/201834672

Høg, E., Fabricius, C., Makarov, V. V., et al. 2000, A&A, 355, L27

Hooton, M. J., Hoyer, S., Kitzmann, D., et al. 2022, A&A, 658, A75, doi: 10.1051/0004-6361/202141645

Ivshina, E. S., & Winn, J. N. 2022, ApJS, 259, 62, doi: 10.3847/1538-4365/ac545b

Jenkins, J. M., Twicken, J. D., McCauliff, S., et al. 2016, in Society of Photo-Optical Instrumentation Engineers (SPIE) Conference Series, Vol. 9913, Software and Cyberinfrastructure for Astronomy IV, ed. G. Chiozzi & J. C. Guzman, 99133E, doi: 10.1117/12.2233418

Kameda, S., Suzuki, H., Takamatsu, T., et al. 2017, SSRv, 208, 17, doi: 10.1007/s11214-015-0227-y

Kameda, S., Yokota, Y., Kouyama, T., et al. 2021, Icarus, 360, 114348, doi: https://doi.org/10.1016/j.icarus.2021.114348

Kawahara, H., Masuda, K., Kotani, T., et al. 2020, in Society of Photo-Optical Instrumentation Engineers (SPIE) Conference Series, Vol. 11443, Space Telescopes and Instrumentation 2020: Optical, Infrared, and Millimeter Wave, ed. M. Lystrup & M. D. Perrin, 1144316, doi: 10.1117/12.2562266

Knapp, M., Seager, S., Demory, B.-O., et al. 2020, AJ, 160, 23, doi: 10.3847/1538-3881/ab8bcc

Kokori, A., Tsiaras, A., Edwards, B., et al. 2022, ApJS, 258, 40, doi: 10.3847/1538-4365/ac3a10

Kokori, A., Tsiaras, A., Edwards, B., et al. 2023, ApJS, 265, 4, doi: 10.3847/1538-4365/ac9da4

Kouyama, T., Tatsumi, E., Yokota, Y., et al. 2021, Icarus, 360, 114353, doi: 10.1016/j.icarus.2021.114353

Krishnamurthy, A., Knapp, M., Günther, M. N., et al. 2021, AJ, 161, 275, doi: 10.3847/1538-3881/abf2c0

Lapeyrere, V., Lacour, S., David, L., et al. 2017, in Proceedings of the 31st Annual AIAA/USU Conference on Small Satellites. https://digitalcommons.usu.edu/smallsat/2017/all2017/86/

Lendl, M., Csizmadia, S., Deline, A., et al. 2020, A&A, 643, A94, doi: 10.1051/0004-6361/202038677

Lillo-Box, J., Figueira, P., Leleu, A., et al. 2020, A&A, 642, A121, doi: 10.1051/0004-6361/202038922

Mandel, K., & Agol, E. 2002, ApJL, 580, L171, doi: 10.1086/345520

Millan, R. M., von Steiger, R., Ariel, M., et al. 2019, Advances in Space Research, 64, 1466, doi: 10.1016/j.asr.2019.07.035

Miller-Ricci, E., Rowe, J. F., Sasselov, D., et al. 2008, ApJ, 682, 593, doi: 10.1086/587634

Mol Lous, M., Weenk, E., Kenworthy, M. A., Zwintz, K., & Kuschnig, R. 2018, A&A, 615, A145, doi: 10.1051/0004-6361/201731941

National Academies of Sciences, Engineering, and Medicine. 2018, Washington, DC: The National Academies Press, doi: 10.17226/25187

Nguyen, T., Morgan, E., Vanderspek, R., et al. 2018, Journal of Astronomical Telescopes, Instruments, and Systems, 4, 047001, doi: 10.1117/1.JATIS.4.4.047001

Nowak, M., Lacour, S., Crouzier, A., et al. 2018, in Society of Photo-Optical Instrumentation Engineers (SPIE) Conference Series, Vol. 10698, Space Telescopes and Instrumentation 2018: Optical, Infrared, and Millimeter Wave, ed. M. Lystrup, H. A. MacEwen, G. G. Fazio, N. Batalha, N. Siegler, & E. C. Tong, 1069821, doi: 10.1117/12.2313242

Nowak, M., Lacour, S., Lapeyrère, V., et al. 2017, arXiv e-prints, arXiv:1708.04015, doi: 10.48550/arXiv.1708.04015

Ogawa, N., Terui, F., Mimasu, Y., et al. 2020, Astrodynamics, 4, 89, doi: 10.1007/s42064-020-0070-0

Parviainen, H. 2015, MNRAS, 450, 3233, doi: 10.1093/mnras/stv894

Patra, K. C., Winn, J. N., Holman, M. J., et al. 2017, AJ, 154, 4, doi: 10.3847/1538-3881/aa6d75

Popowicz, A. 2018, Sensors, 18, 479, doi: 10.3390/s18020479

Ricker, G. R., Winn, J. N., Vanderspek, R., et al. 2015, Journal of Astronomical Telescopes, Instruments, and Systems, 1, 014003, doi: 10.1117/1.JATIS.1.1.014003

Sarda, K., Grant, C., Chaumont, M., et al. 2014, in Proceedings of the 28th Annual AIAA/USU Conference on Small Satellites (SmallSat). https://digitalcommons.usu.edu/smallsat/2014/YearReview/4/

Serjeant, S., Elvis, M., & Tinetti, G. 2020, Nature Astronomy, 4, 1031, doi: 10.1038/s41550-020-1201-5

Shkolnik, E. L. 2018, Nature Astronomy, 2, 374, doi: 10.1038/s41550-018-0438-8

Smith, M., Donner, A., Knapp, M., et al. 2018, in Proceedings of the 32nd Annual AIAA/USU Conference on Small Satellites. https://digitalcommons.usu.edu/smallsat/2018/all2018/255/

Sreejith, A. G., France, K., Fossati, L., et al. 2023, ApJL, 954, L23, doi: 10.3847/2041-8213/acef1c

Suzuki, H., Yamada, M., Kouyama, T., et al. 2018, Icarus, 300, 341, doi: 10.1016/j.icarus.2017.09.011

Talens, G. J. J., Albrecht, S., Spronck, J. F. P., et al. 2017, A&A, 606, A73, doi: 10.1051/0004-6361/201731282

Tatsumi, E., Kouyama, T., Suzuki, H., et al. 2019, Icarus, 325, 153, doi: 10.1016/j.icarus.2019.01.015

Tsuda, Y., Ono, G., Saiki, T., et al. 2017, Journal of Spacecraft and Rockets, 54, 1284

Twicken, J. D., Caldwell, D. A., Jenkins, J. M., et al. 2020,

Van Grootel, V., Pozuelos, F. J., Thuillier, A., et al. 2021, A&A, 650, A205, doi: 10.1051/0004-6361/202140381

Vanderspek, R., Doty, J., Fausnaugh, M., et al. 2018,

Walker, G., Matthews, J., Kuschnig, R., et al. 2003, PASP, 115, 1023, doi: 10.1086/377358

Weiss, W. W., Zwintz, K., Kuschnig, R., et al. 2021, Universe, 7, 199, doi: 10.3390/universe7060199

Whittaker, G. N. 2014, PhD thesis, University of Birmingham

Winn, J. N., Matthews, J. M., Dawson, R. I., et al. 2011, ApJL, 737, L18, doi: 10.1088/2041-8205/737/1/L18

Wraight, K. T., White, G. J., Bewsher, D., & Norton, A. J. 2011, MNRAS, 416, 2477, doi: 10.1111/j.1365-2966.2011.18599.x

Yeh, L.-C., & Jiang, I.-G. 2020, PASP, 133, 014401, doi: 10.1088/1538-3873/abbb24

Yumoto, K., Tatsumi, E., Kouyama, T., et al. 2024, Icarus, 417, 116122, doi: 10.1016/j.icarus.2024.116122